International Journal of Heat and Mass Transfer 52 (2009) 5759–5769

Contents lists available at ScienceDirect

International Journal of Heat and Mass Transfer

journal homepage: www.elsevier.com/locate/ijhmt

Effect of surface radiation on conjugate natural convection in a horizontal annulus driven by inner heat generating solid cylinder

A. Shaija, G.S.V.L. Narasimham *

Department of Mechanical Engineering, Indian Institute of Science, Bangalore 560 012, India

ARTICLE INFO

Article history:
Received 16 July 2008
Received in revised form 16 March 2009
Accepted 22 May 2009
Available online 8 September 2009

Keywords:
Horizontal annuli
Volumetric heat generation
Non-staggered grid
Surface radiation
Radiation Nusselt number
Convection Nusselt number

ABSTRACT

This paper reports a numerical study of the laminar conjugate natural convection heat transfer with and without the interaction of the surface radiation in a horizontal cylindrical annulus formed between an inner heat generating solid circular cylinder and an outer isothermal circular boundary. Numerical solutions are obtained by solving the governing equations with a pressure correction method on a collocated (non-staggered) mesh. Steady-state results are presented for the flow and temperature distributions and Nusselt numbers for the heat generation based Grashof number ranging from 10^7 to 10^{10}, solid-to-fluid thermal conductivity ratios of 1, 5, 10, 50 and 100, radius ratios of 0.226 and 0.452 and surface emissivities of 0–0.8 with air as the working medium. It is observed that surface radiation reduces the convective heat transfer in the annulus compared to the pure natural convection case and enhances the overall Nusselt number.

1. Introduction

Though the amount of research done on natural convection in annular cavities is considerable, relatively less number of publications, that take into consideration the contribution of surface radiation, have appeared. Conjugate natural convection heat transfer in the presence of surface radiation in annular cavities bounded by co-axial, horizontal circular cylinders has not been investigated widely in the past despite its technological applications such as transportation and storage of spent nuclear fuel casks, underground transmission cables, heat transfer in nuclear reactors, cooling of electrical and electronic components, solar heat collection using concentrators, heat removal from gas-cooled fast reactors, design of high-temperature heat exchangers, etc. The presence of surface radiation modifies the velocity and temperature fields in the annulus and the magnitude of the convective coefficients.

A number of investigations have been reported on the natural convection heat transfer in a horizontal cylindrical annulus. For instance, Kuehn and Goldstein [1–3] have conducted both a finite difference numerical simulation and an experimental study using Mach–Zehnder interferometer to determine the influence of Rayleigh number, Prandtl number, diameter ratio on the temperature distributions and the local equivalent conductivities on the inner and outer cylinders. Kuehn and Goldstein [4] have also presented a correlation for natural convection heat transfer between horizontal circular cylinders. Grigull and Hauf [5] have measured the temperature field in the gap between two horizontal isothermal cylinders filled with air and local heat transfer coefficients on the inner cylinder for nine diameter ratios using a Mach–Zehnder interferometer. They have categorized the flow patterns into pseudo-conductive, transition and fully developed convection regimes. Rotem [6] has studied the conjugate free convection in a horizontal annulus using a series expansion technique. The inner solid cylinder carried either a line source along its axis or a distributed heat source or both and the outer cylinder is maintained at a constant temperature. Bubnovich and Kolesnikov [7], Kolesnikov and Bubnovich [8] and Lacroix and Joyeux [9] have numerically studied the conjugate problem of natural convection in horizontal annuli to investigate the influence of the finite conductance of the cylinder walls.

The interaction of surface radiation and natural convection in rectangular enclosures has received some attention in the literature. For instance, Balaji and Venkateshan [10] have numerically investigated the interaction of surface radiation and natural convection in a square cavity. The combined convection and radiation problem has been studied by Balaji and Venkateshan [11] for an open cavity with air as the intervening medium for the Rayleigh number range 10^4–10^8. It is found that the radiation has a dual effect of contributing to the overall heat transfer as well as decreasing the convective component. Correlations based on the numerical results were presented for both convection and radiation. The experimental work of Ramesh and Merzkirch [12] on combined natural convection and radiation in an open cavity

---

* Corresponding author. Tel.: +91 80 22932971; fax: +91 80 23600648.
E-mail address: mecgsvln@mecheng.iisc.ernet.in (G.S.V.L. Narasimham).

0017-9310/$ - see front matter © 2009 Elsevier Ltd. All rights reserved.
doi:10.1016/j.ijheatmasstransfer.2009.05.033

Nomenclature

c	specific heat capacity (J kg^{-1} K^{-1})
C_c	correlation coefficient $(= 1 - e_{ms}/\sigma^2)$
e_{ms}	mean square error
F	radiation configuration factor
g	acceleration due to gravity (m s^{-2})
G	irradiation (W m^{-2})
Gr	heat generation based Grashof number $[= (g\beta\Delta T R_o^3)/\nu_f^2,\ \Delta T = \dot{Q}_v R_o^2/\lambda_f]$
i, j	grid point indices
J	radiosity (W m^{-2})
$Nu_{pnc,av,ib}$	average convective Nusselt number for the inner boundary (pure convection)
$Nu_{c,av,ib}$	average convective Nusselt number for the inner boundary (with radiative effect)
$Nu_{r,av,ib}$	average radiative Nusselt number for the inner boundary
Nu_t	total Nusselt number
P	perimeter (m)
Pr	Prandtl number
P_{rc}	radiation–conduction parameter
$\dot{q}$	heat flux (W m^{-2})
$\dot{Q}_v$	volumetric heat generation (W m^{-3})
R_i, R_o	radii of the inner and outer cylinders, respectively (m)
R_{oh}	overheat ratio
Ra	Rayleigh number $(= Gr \cdot Pr)$
t	time (s)
T	temperature (K)
v_r, v_θ	velocities in the radial and tangential directions (m s^{-1})

Greek symbols

α	heat transfer coefficient (W m^{-2} K^{-1})
β	volumetric expansion coefficient (K^{-1})
$\delta_{k,j}$	Kronecker delta
ϵ	emissivity
η	dynamic viscosity (Pa s)
θ	angular coordinate (rad)
κ	radius ratio (R_i/R_o)
λ	thermal conductivity (W m^{-1} K^{-1})
ν	kinematic viscosity (m^2 s^{-1})
ξ	distance along cylinder surface (m)
ρ	density (kg m^{-3})
σ	Stefan–Boltzmann constant (W m^{-2} K^{-4})
ψ	stream function $[= \int(r v_r d\theta - v_\theta dr)]$ (m^2 s^{-1})

Subscripts

av	average
c	convective
eq	equivalent
f, s	fluid and solid, respectively
ib, ob	inner and outer boundaries, respectively
j, k	subsurfaces
l	local
max	maximum
p	constant pressure
pnc	pure natural convection
r	radiative
ref	reference
t	total (i.e., convective plus radiative)

Superscript

$*$	dimensionless quantity

geometry with an active isothermal longer vertical wall, insulated shorter opposing wall and an insulated horizontal bottom wall indicates that the radiation contribution increases from about 5% to 50% when the wall emissivity increases from 0.05 to 0.85. The numerical analysis for this problem was performed by Singh and Venkateshan [13]. Anil et al. [14] studied the conjugate turbulent natural convection and surface radiation in rectangular enclosures and investigated the effect of Rayleigh number, aspect ratio, wall emissivity and the external heat transfer coefficient on the heat transfer.

Literature on natural convection in circular geometries in the presence of radiation is very limited. Perlmutter and Howell [15] have obtained solutions for the radiation heat transfer and emissive power distribution between infinitely long concentric gray cylinders at different wall temperatures and emissivities enclosing a gray non-isothermal gas with a uniformly distributed heat source using Monte Carlo method. Onyegegbu [16] has studied analytically the heat transfer in an absorbing and emitting non-gray Boussinésq fluid within the annular gap of two infinitely long isothermal horizontal concentric cylinders using the Milne–Eddington approximation.

The objective of the present work is to numerically investigate the coupled conduction, natural convection and surface radiation inside a horizontal annulus. The annulus is formed by an inner heat generating solid circular cylinder and an isothermal concentric outer boundary. Such problems arise in several applications. For instance, spent nuclear fuel casks contain one or more canisters of circular cross-section in which bundles of spent fuel rods are packed. The canister can often be modelled as a heat generating solid with an equivalent thermal conductivity. Due to close spacings, the mode of heat transmission through the fill gas is often conduction. Methods of calculating equivalent thermal conductivity of such arrays of tubes or rods have been presented by Manteufel and Todreas [17].

2. Mathematical formulation

2.1. The physical model and the coordinate system

The physical model comprises a heat generating inner solid circular cylinder EFGHE of radius R_i enclosed by an outer concentric circular boundary ABCDA of radius R_o, as shown in Fig. 1.

The problem is described in plane cylindrical coordinates with the gravity vector acting vertically downwards. $\hat{e}_r$ and $\hat{e}_\theta$ are the unit vectors along r- and θ-directions, respectively. The angle θ is measured from OB in the counter-clockwise direction. The annulus is assumed to be sufficiently long so that the flow and temperature fields can be taken as invariant along the z-direction, neglecting the end effects.

At times less than or equal to zero, the fluid inside the annulus is quiescent with uniform temperature at T_{ref}. For times greater than zero, the inner solid square begins to generate heat with a volumetric heat generation rate of $\dot{Q}_v$, which is transferred to the fluid, whereas the outer cylinder is isothermally cooled with the temperature maintained at $T_o = T_{ref}$.

2.2. Governing equations

The flow and temperature distributions are assumed to be two-dimensional and are governed by continuity, Navier–Stokes, fluid

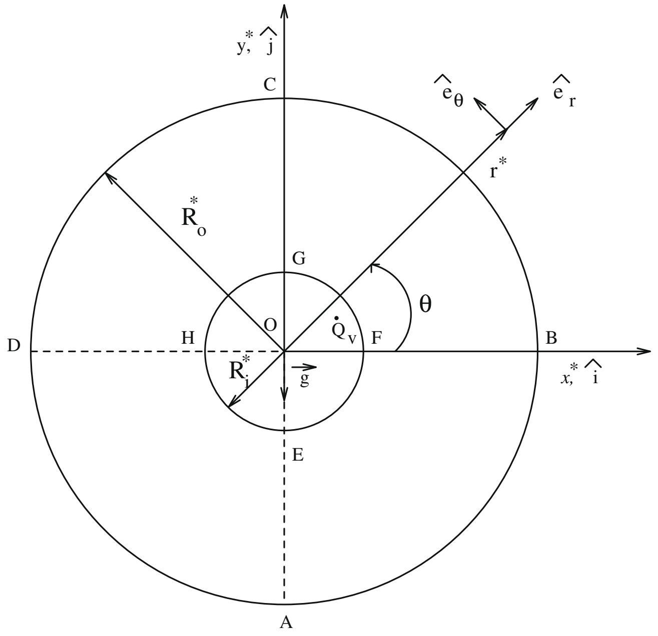

Fig. 1. The physical model and coordinate system for the annulus.

and solid energy equations and the surface radiative heat transfer coupling at the inner and outer boundaries. The viscous dissipation and compressibility effects are considered to be negligible. The effect of density variation causing the buoyancy force is taken into account through the Oberbeck–Boussinésq approximation. Other thermophysical properties of the fluid and those of the solid are assumed to be independent of temperature. The inner surface of the outer cylinder and the surface of the inner cylinder are assumed to be diffuse and gray, i.e., the emissivity and absorptivity are independent of wavelength. The governing equations in dimensionless form read:

Continuity equation:

$$\frac{\partial(r^* v^*_r)}{\partial r^*} + \frac{\partial v^*_\theta}{\partial \theta} = 0 \tag{1}$$

Momentum equation in r-direction:

$$\begin{aligned}&\frac{\partial v^*_r}{\partial t^*} + \frac{1}{r^*}\frac{\partial(r^* v^*_r v^*_r)}{\partial r^*} + \frac{1}{r^*}\frac{\partial(v^*_\theta v^*_r)}{\partial \theta}\\ &\quad = -\frac{\partial p^*}{\partial r^*} + \frac{1}{r^*}\frac{\partial}{\partial r^*}\left(r^*\frac{\partial v^*_r}{\partial r^*}\right) + \frac{1}{r^*}\frac{\partial}{\partial \theta}\left(\frac{1}{r^*}\frac{\partial v^*_r}{\partial \theta}\right) + S^*_{vr}\end{aligned} \tag{2}$$

$$\begin{aligned}S^*_{vr} &= \frac{1}{r^*}\frac{\partial}{\partial r^*}\left(r^*\frac{\partial v^*_r}{\partial r^*}\right) + \frac{1}{r^*}\frac{\partial}{\partial \theta}\left(\frac{\partial v^*_\theta}{\partial r^*}\right) - \frac{1}{r^*}\frac{\partial}{\partial \theta}\left(\frac{v^*_\theta}{r^*}\right)\\ &\quad - \frac{2}{r^{*2}}\left(\frac{\partial v^*_\theta}{\partial \theta} + v^*_r\right) + \frac{v^{*2}_\theta}{r^*} + GrT^* \sin\theta\end{aligned} \tag{3}$$

Momentum equation in θ-direction:

$$\begin{aligned}&\frac{\partial v^*_\theta}{\partial t^*} + \frac{1}{r^*}\frac{\partial(r^* v^*_r v^*_\theta)}{\partial r^*} + \frac{1}{r^*}\frac{\partial(v^*_\theta v^*_\theta)}{\partial \theta}\\ &\quad = -\frac{1}{r^*}\frac{\partial p^*}{\partial \theta} + \frac{1}{r^*}\frac{\partial}{\partial r^*}\left(r^*\frac{\partial v^*_\theta}{\partial r^*}\right) + \frac{1}{r^*}\frac{\partial}{\partial \theta}\left(\frac{1}{r^*}\frac{\partial v^*_\theta}{\partial \theta}\right) + S^*_{v\theta}\end{aligned} \tag{4}$$

$$\begin{aligned}S^*_{v\theta} &= \frac{1}{r^*}\frac{\partial}{\partial r^*}\left(\frac{\partial v^*_r}{\partial \theta} - v^*_\theta\right) + \frac{1}{r^*}\frac{\partial}{\partial \theta}\left[\frac{1}{r^*}\left(\frac{\partial v^*_\theta}{\partial \theta} + 2v^*_r\right)\right]\\ &\quad + \frac{1}{r^*}\left(\frac{\partial v^*_\theta}{\partial r^*} + \frac{1}{r^*}\frac{\partial v^*_r}{\partial \theta} - \frac{v^*_\theta}{r^*}\right) - \frac{v^*_r v^*_\theta}{r^*} + GrT^* \cos\theta\end{aligned} \tag{5}$$

where S^*_{vr} and $S^*_{v\theta}$ are the source terms in the r-momentum and θ-momentum equations, respectively.

Energy equation for the fluid:

$$\begin{aligned}&\frac{\partial T^*_f}{\partial t^*} + \frac{1}{r^*}\frac{\partial}{\partial r^*}(r^* v^*_r T^*_f) + \frac{1}{r^*}\frac{\partial}{\partial \theta}(v^*_\theta T^*_f)\\ &\quad = \frac{1}{r^* Pr}\left[\frac{\partial}{\partial r^*}\left(r^*\frac{\partial T^*_f}{\partial r^*}\right) + \frac{\partial}{\partial \theta}\left(\frac{1}{r^*}\frac{\partial T^*_f}{\partial \theta}\right)\right]\end{aligned} \tag{6}$$

Energy equation for the solid:

$$\rho^*_s c^*_s \frac{\partial T^*_s}{\partial t^*} = \frac{\lambda^*_s}{r^* Pr}\left[\frac{\partial}{\partial r^*}\left(r^*\frac{\partial T^*_s}{\partial r^*}\right) + \frac{\partial}{\partial \theta}\left(\frac{1}{r^*}\frac{\partial T^*_s}{\partial \theta}\right)\right] + \frac{1}{Pr} \tag{7}$$

where λ^*_s is the solid-to-fluid thermal conductivity ratio.

The system of non-dimensionalisation is:

$$\begin{aligned}&r^* = \frac{r}{R_o}, \quad v^*_r = \frac{v_r R_o}{\nu_f}, \quad v^*_\theta = \frac{v_\theta R_o}{\nu_f}, \quad t^* = \frac{t\nu_f}{R_o^2}, \quad \rho^*_s = \frac{\rho_s}{\rho_f},\\ &c^*_s = \frac{c_s}{c_{p,f}}, \quad \lambda^*_s = \frac{\lambda_s}{\lambda_f}, \quad Gr = \frac{g\beta\Delta T R_o^3}{\nu_f^2}, \quad T^* = \frac{(T - T_{ref})}{\Delta T},\\ &\Delta T = \frac{\dot{Q}_v R_o^2}{\lambda_f}, \quad Pr = \frac{\eta_f c_{p,f}}{\lambda_f}\end{aligned} \tag{8}$$

2.3. Relations for surface radiation heat exchange

Since natural convection and radiation are being simultaneously computed, the inner and outer surface segments formed by the computational mesh are taken as the subsurfaces for the calculation of radiative heat exchange. The radiative heat flux $\dot{q}_{r,k}$ leaving a subsurface k in an enclosure is related to the irradiation G_k of the subsurface (i.e., the total heat flux falling on the subsurface) and the radiosity J_k (i.e., the sum of the heat flux emitted and reflected from a subsurface), through the relation:

$$\dot{q}_{r,k} = J_k - G_k = \frac{\epsilon_k}{1 - \epsilon_k}(\dot{E}_{b,k} - J_k) \tag{9}$$

where $\dot{E}_{b,k} = \sigma T_k^4$ is the black body emissive power, T_k is the absolute temperature and ϵ_k is the emissivity of the kth subsurface. The irradiation is given by:

$$G_k = \frac{1}{A_k}\sum_{j=1}^{N} J_j A_j F_{j,k} \tag{10}$$

where $F_{j,k}$ is the radiation configuration factor between subsurfaces j and k, determined by Hottel's crossed string method [18,19]. Each of the subscripts k and j varies from 1 to N, (N = total number of subsurfaces in the enclosure) and A_j and A_k are the areas of the respective subsurfaces. The method of calculating the radiation configuration factors is presented in Section 2.6.

Using Eq. (10) in Eq. (9), the following relation is obtained for the kth surface:

$$\sum_{j=1}^{N}\left[\frac{\delta_{k,j}}{(1 - \epsilon_j)} - F_{j,k}\right] A_j J_j = \frac{\epsilon_k}{1 - \epsilon_k} A_k \sigma T_k^4 \tag{11}$$

where $\delta_{k,j}$ is the Kronecker delta and σ is the Stefan–Boltzmann constant.

The above equation in dimensionless form reads:

$$\sum_{j=1}^{N}\left[\frac{\delta_{k,j}}{(1 - \epsilon_j)} - F_{j,k}\right] A^*_j J^*_j = \frac{\epsilon_k}{1 - \epsilon_k} A^*_k P_{rc} \frac{(1 + T^*_k R_{oh})^4}{R_{oh}} \tag{12}$$

where $R_{oh} = \Delta T_c / T_c$ is the overheat ratio and $P_{rc} = \sigma T_c^3 R_o / \lambda_c$ is the radiation–conduction parameter. The dimensionless radiosity is defined as $J^*_k = (J_k R_o)/(\lambda_f \Delta T_c)$.

By writing Eq. (12) for all the subsurfaces, a set of simultaneous equations is obtained, which in matrix notation is expressed as:

$$[C][J^*] = [B], \text{ i.e., } [J^*] = [C]^{-1}[B] \tag{13}$$

The general elements in the above coefficient matrix and the forcing vector can be obtained by correspondence with Eq. (12).

The solution of the simultaneous equations yields the radiosity values for all the subsurfaces. The net dimensionless radiation flux leaving the subsurface k is given by:

$$\dot{q}^*_{\mathrm{r},k} = \frac{\epsilon_k}{1-\epsilon_k}\left[P_{\mathrm{rc}}\frac{(1+T^*_k R_{\mathrm{oh}})^4}{R_{\mathrm{oh}}} - J^*_k\right] \tag{14}$$

To take into account the coupling between natural convection and surface radiation, a correspondence is established between the grid and subsurface numbering schemes. It is assumed that the subsurface has a uniform flux over its extent, equal to the local net radiation flux at the grid point contained in it.

The parameters of the problem are the heat generation based Grashof number (Gr), solid-to-fluid thermal conductivity ratio (λ^*_{s}), radius ratio (κ), Prandtl number (Pr), emissivity of the inner and the outer boundaries (ϵ), radiation–conduction parameter (P_{rc}) and the overheat ratio (R_{oh}). Thus the dimensionless temperatures of interest and the average Nusselt number will be functions of these parameters. For instance, $Nu = F(Gr, \lambda^*_{\mathrm{s}}, \kappa, Pr, \epsilon, R_{\mathrm{oh}}, P_{\mathrm{rc}})$.

2.4. Initial and boundary conditions

The initial conditions at $t^* = 0$ correspond to a quiescent state with uniform temperature. At $t^* > 0$, no-slip hydrodynamic condition exists on the inner and outer boundaries of the annulus. The thermal boundary conditions at the solid–fluid interface are the heat flux continuity and no temperature jump. The heat flux continuity includes the radiation heat flux $\dot{q}^*_{\mathrm{r},k}$ leaving the inner surface in the fluid region, which can be written as:

$$-\lambda^*_{\mathrm{s}}\frac{\partial T^*_{\mathrm{s}}}{\partial n^*_{\mathrm{s}}} = -\frac{\partial T^*_{\mathrm{f}}}{\partial n^*_{\mathrm{f}}} + \dot{q}^*_{\mathrm{r},k}, \quad T^*_{\mathrm{s}} = T^*_{\mathrm{f}} \tag{15}$$

where n^*_{s} is the dimensionless normal distance measured in the solid towards the interface and n^*_{f} is the dimensionless normal distance measured in the fluid from the interface.

2.5. Nusselt numbers

The local, inner boundary, convective Nusselt number $Nu_{\mathrm{l,ib,c}}$, with respect to the temperature difference $(T_{\mathrm{av,ib}} - T_{\mathrm{o}})$ is:

$$Nu_{\mathrm{l,ib,c}} \equiv \frac{\alpha_{\mathrm{l,ib,c}} R_{\mathrm{o}}}{\lambda_{\mathrm{f}}} = -\frac{1}{T^*_{\mathrm{av,ib}}}\left[\frac{\partial T^*_{\mathrm{f}}}{\partial n^*_{\mathrm{f}}}\right]_{\mathrm{l,ib,c}} = \frac{\dot{q}^*_{\mathrm{l,ib,c}}}{T^*_{\mathrm{av,ib}}} \tag{16}$$

where $\dot{q}^*$, the dimensionless heat flux, is $(\dot{q}R_{\mathrm{o}})/(\lambda_{\mathrm{f}}\Delta T_{\mathrm{c}})$.

Similarly, the local, inner boundary, radiative Nusselt number $Nu_{\mathrm{l,ib,r}}$ is:

$$Nu_{\mathrm{l,ib,r}} \equiv \frac{\alpha_{\mathrm{l,ib,r}} R_{\mathrm{o}}}{\lambda_{\mathrm{f}}} = \frac{\dot{q}^*_{\mathrm{l,ib,r}}}{T^*_{\mathrm{av,ib}}} \tag{17}$$

The average convective Nusselt number $Nu_{\mathrm{c,av,ib}}$ (in the presence of radiation effects) and the average radiative Nusselt number $Nu_{\mathrm{r,av,ib}}$ on the inner boundary are given by:

$$Nu_{\mathrm{c,av,ib}} = \frac{1}{P^*_{\mathrm{ib}}}\int_{\mathrm{ib}} Nu_{\mathrm{l,ib,c}}\, d\xi^*_{\mathrm{ib}}, \quad Nu_{\mathrm{r,av,ib}} = \frac{1}{P^*_{\mathrm{ib}}}\int_{\mathrm{ib}} Nu_{\mathrm{l,ib,r}}\, d\xi^*_{\mathrm{ib}} \tag{18}$$

where P^*_{ib} and $T^*_{\mathrm{av,ib}}$ are the dimensionless perimeter and the dimensionless average temperature on the inner boundary.

The Nusselt numbers on the outer boundary are defined in a similar manner. Both P^*_{ib} and P^*_{ob} are measured from the bottommost point of the respective boundaries in a counter-clockwise direction.

The total Nusselt number, Nu_{t} on the inner boundary is the sum of convective Nusselt number with the influence of radiation and the radiative Nusselt number.

$$Nu_{\mathrm{t}} = Nu_{\mathrm{c,av,ib}} + Nu_{\mathrm{r,av,ib}} \tag{19}$$

2.6. Calculation of configuration factors

To find the configuration factor between the segment AD on the inner surface and the segment BC on the outer surface by Hottel's crossed string method, strings are imagined to be stretched among each pair in the set of points A, B, C and D, which are consecutively designated in a counter-clockwise direction. AD can view the arc PS (counter-clockwise) of the outer circle. The configuration factor between AD and any subsurface on the rest of the outer circumference is zero. In Fig. 2, point B or C is shown. Ox is the initial line from which the angle made by any radius vector is measured counter-clockwise. With respect to B, C will be ahead on the outer surface in a counter-clockwise direction; with respect to C, B will be behind. AB and CD are the straight strings, and AC and BD are the crossed strings. The semi-tangents at A are AP and AR, and the semi-tangents at D are DQ and DS. If point B lies between P and Q, the crossed string BD consists of a straight portion BE $\left(= \sqrt{R^{*2}_{\mathrm{o}} - R^{*2}_{\mathrm{i}}}\right)$ and a wrap ED around the inner circle. The angle subtended by BE at the center is $\cos^{-1}(R^*_{\mathrm{i}}/R^*_{\mathrm{o}})$. The wrap is given by $R^*_{\mathrm{i}}(\theta_{\mathrm{D}} - \theta_{\mathrm{E}})$, where $\theta_{\mathrm{E}} = \theta_{\mathrm{B}} - \cos^{-1}(R^*_{\mathrm{i}}/R^*_{\mathrm{o}})$. The variation of the difference between any two angles is limited to the range 0—2π. This requires the addition or subtraction of 2π where the original difference is less than zero or greater than 2π. If point C lies between P and Q, the straight string CD consists of a straight portion CE and a wrap ED around the inner circle. Similarly depending on B or C lying between R and S, the straight string AB or the crossed string CA will have a wrap. If B or C lies between Q and R, the corresponding strings will not have any wrap around the inner surface. If P or S lies inside the outer subsurface BC, the fact that the arc AD can see only the portion PC or BS should be taken into account while determining the radiation configuration factor $F_{\mathrm{AD-BC}}$. Since reciprocity is not valid for such part-view surfaces,

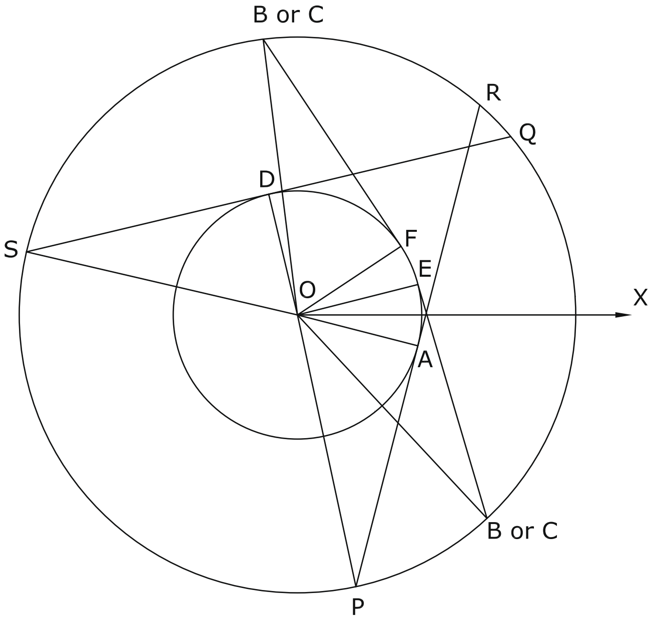

Fig. 2. Radiation configuration factors between inner-to-outer boundary subsurfaces.

all the configuration factors are individually calculated without making use of the reciprocity rule. With the lengths of the strings determined, the quantity $L_{AD} \cdot F_{AD-BC}$ is given by half the difference between the sum of the crossed strings and the sum of the straight strings, where L_{AD} is the arc length AD.

Fig. 3 shows the method of calculating the configuration factor between the outer subsurface AB and a subsurface CD, with A, B, C and D consecutively designated in a counter-clockwise direction. The configuration factor is outer-to-inner or outer-to-outer according as CD is the inner or outer element. AB can see the portion PS (counter-clockwise) on the inner circle and the portion EH (counter-clockwise) on the outer circle. If CD is an inner subsurface, the wrap that occurs to a straight or crossed string when C or D lies between P and Q or R and S, is to be taken into account. If CD is an outer subsurface, a straight or crossed string can have two straight portions and a wrap when C or D lies between E and F or G and H. Other considerations are similar to the method of finding inner-to-outer configuration factor.

3. Numerical formulation

3.1. Pressure–velocity coupling

The governing equations are solved in primitive form on a collocated mesh. Among the algorithms for incompressible flow primitive variable formulations, the SIMPLE (Semi-Implicit Method for Pressure-Linked Equations) algorithm has been employed frequently along with a staggered grid. However, for complex geometries, non-uniform meshes and three-dimensional cases, the use of a staggered mesh increases the storage requirements, programming effort and the computation time [20]. In the present work, SIMPLE procedure is implemented on collocated grids, where the velocities and other scalars are defined at the same node. This method employs the same control volume for pressure, velocity and temperature and the discretized equations are similar for all variables. This solution methodology saves computer time and may provide faster convergence for some problems. Direct application of the SIMPLE algorithm to collocated meshes can result in checkerboard splitting of the pressure field, because the face velocities are expressed in terms of the pressure difference between two alternating, rather than consecutive nodes. The present problem is solved using the algorithms suggested by Perić et al. [20], Armfield [21] and Date [22,23], respectively, and the maximum dimensionless temperatures and the Nusselt numbers are compared.

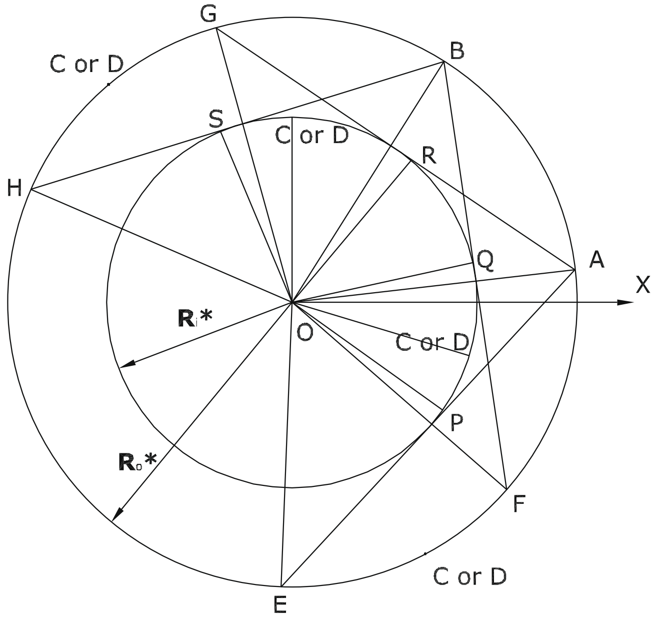

Fig. 3. Radiation configuration factors between outer-to-inner and outer-to-outer boundary subsurfaces.

3.2. Discretization

The convective terms in the governing equations are discretized by the donor-cell method (Torrance and Rockett [24] and Vafai and Ettefagh [25]) and the diffusive terms by the central differences using second-order accurate analogues. The heat flux continuity condition is discretized using two-point one-sided differences. The local fluid temperature gradients are evaluated with third-order accurate finite difference representations on the inner and outer boundaries. In order to resolve the center point singularity, the solid energy equation in cartesian form is discretized at the center of the inner solid circle with the first grid circle radius as the mesh spacing. Choosing the number of the angular spacings as a multiple of four, such discretized equations are written for all the required mutually perpendicular orientations of the radial lines and are summed up. The relation for the center temperature is obtained from the summed up discretized equations.

3.3. Solution procedure

Steady-state results are obtained as the long-time solutions to time-dependent equations using finite difference techniques. A segregated solution approach is adopted, which, for each global iteration, consists in succession, the solution of the radial and tangential direction momentum equations, pressure correction equation and the energy equations with velocity and pressure corrections carried out before the solution of the energy equations. For each iteration of an equation, the solution is obtained by a θ-direction sweep with the application of the tri-diagonal matrix algorithm for the grid points on each radial line.

For determining the radiosity values, the inverse matrix $[C]^{-1}$ in Eq. (13) is computed only once by the Gauss–Jordan method with partial pivoting and stored. Subsequently, the radiosity values are obtained by multiplying the forcing vector with the inverse matrix.

Sufficient number of global iterations on the set of equations are performed over each time step for better coupling of the velocity and temperature fields. The time step is chosen as a multiple (typically 50) of that obtained from the combined Courant–Friedrichs–Lewy and diffusion number restrictions applicable to explicit methods (Roache [26]). A relative convergence criterion of 5×10^{-5} on the maximum dimensionless temperature is chosen for the global iteration process at each time step. The criterion for the attainment of steady state is that the relative difference of the maximum temperature in the domain over a large number of time steps (50–100) should be less than 5×10^{-5}. The energy balances on the inner and outer boundaries with respect to the total heat generation are used as additional checks for the attainment of steady state. The integral energy balance can be written as:

$$\dot{Q}_z^* = \int_{\mathrm{ib}} \left[-\left(\frac{\partial T^*}{\partial r^*} \right)_{\mathrm{l,ib}} + \dot{q}^*_{\mathrm{l,ib,r}} \right] d\xi^*_{\mathrm{ib}} = \int_{\mathrm{ob}} \left[-\left(\frac{\partial T^*}{\partial r^*} \right)_{\mathrm{l,ob}} - \dot{q}^*_{\mathrm{l,ob,r}} \right] d\xi^*_{\mathrm{ob}} \tag{20}$$

where $\dot{Q}_z^* = \dot{Q}_z/(\lambda_f \Delta T_c)$, the dimensionless heat generation per unit length in the inner solid cylinder, is πR_i^{*2}.

The heat transfer rates across the inner and outer boundaries are obtained by integration of the local fluid temperature gradient around the respective peripheries. The numerical quadrature is performed using the high-accuracy scheme of Gill and Miller

[27]. To obtain faster convergence to steady state, the quantity $\rho_s^* c_s^*$ is set equal to unity.

A computer program is developed and run on the ALPHA work stations at the Supercomputer Education and Research Center, Indian Institute of Science, Bangalore, India. All the calculations are performed with the double-precision arithmetic, for which the word length is 32 bits.

3.4. Validation of the computer program

The collocated mesh method is first validated with the benchmark results of de Vahl Davis [28] and Hortmann et al. [29], reported for the buoyancy-driven flow in a differentially heated cavity with top and bottom sides insulated, as shown in Table 1. Secondly, the steady-state results of the natural convection in the horizontal annulus are compared with those obtained from vorticity–stream function approach. The results agree well with each other with a maximum difference of about 6% in the dimensionless maximum temperature and average Nusselt number on the inner boundary.

3.5. Grid sensitivity tests

To see the effect of mesh size on the conjugate results, computations are carried out with five different meshes with the number of mesh spacings varying from 60 to 100 in each direction. An 81×80 mesh is finally chosen with equal number of mesh spacings in the radial and angular directions. This grid contains 33 and 41 grid points in the solid region for $\kappa = 0.226$ and 0.452, respectively. To ensure grid compatibility, the same subsurfaces on the inner and outer boundaries are used for radiative heat exchange calculations.

4. Results and discussion

As the first part of the investigation, steady-state results for the conjugate problem with pure natural convection are computed with the algorithms formulated by Perić et al. [20], Armfield [21] and Date [22,23] for Grashof number, $Gr = 10^8$, solid-to-fluid thermal conductivity ratio (λ_s^*) of 10 and 50 and the radius ratios (κ) of 0.226 and 0.452 and the results are presented in Table 2. The κ values considered are 0.226 and 0.452, which correspond to inner circles equal in area to squares of sides 0.4 and 0.8, respectively. It could be seen that there is only a negligible variation in the pure convection quantities like average Nusselt Number on the inner boundary ($Nu_{\mathrm{pnc,av,ib}}$), average Nusselt Number on the outer boundary ($Nu_{\mathrm{pnc,av,ob}}$), average dimensionless inner boundary temperature ($T^*_{\mathrm{pnc,av,ib}}$) and maximum dimensionless temperature ($T^*_{\mathrm{pnc,max}}$) when different algorithms are employed. Hence, most of the results are obtained with the algorithm of Perić et al. [20].

Secondly, steady-state results for the conjugate problem with pure natural convection and for the combined case (taking radiation effects) are computed for Gr range 10^7–10^{10}, λ_s^* of 1, 5, 10, 50 and 100, and κ of 0.226 and 0.452 using the algorithm formulated by Perić et al. [20].

Choosing $R_o = 0.25$ m and the cold reference temperature as $T_{\mathrm{ref}} = 300$ K, for air as the working fluid, both the Grashof number (Gr) and the overheat ratio (R_{oh}) become functions of volumetric heat generation rate, $\dot{Q}_v$. Hence, by varying $\dot{Q}_v$, both Gr and R_{oh} change. For instance, when $\dot{Q}_v$ varies from 2.3 W m^{-3} to 2300 W m^{-3}, Gr varies between 10^7 and 10^{10} and R_{oh} varies from 0.0178 to 17.87. The chosen value of R_o, namely, 0.25 m, finds application in test or pilot reactor spent nuclear fuel casks. The radiation–conduction parameter P_{rc} is kept constant at 14.89. The heat generation and outer radius based Grashof number Gr is generally two to three orders of magnitude higher than Grashof number Gr_T, based on the difference between the average inner boundary and the outer boundary temperatures, and hence the flow is found to remain laminar even for Gr values as high as 10^{10}. The quantity Gr_T is defined as $[g\beta(T_{\mathrm{av,ib}} - T_{\mathrm{ref}})R_o^3]/\nu_f^2$. Since the computations cover a wide parametric space, selected results are presented.

Table 1

Comparison of the present results with the benchmark results for the average Nusselt number on the vertical walls of the enclosure.

Ra	de Vahl Davis [28]	Hortmann et al. [29]	Present
10^5	4.519	4.525	4.513
10^6	8.800	8.851	8.829

4.1. Isotherms and streamlines

The isotherm (right half) and streamline (left half) maps for $\lambda_s^* = 10,\ \kappa = 0.226$ and for Gr ranging from 10^7 to 10^{10} for pure natural convection (a–d) and for combined convection and radiation (e–h) are shown in Fig. 4 (The stream function ψ is defined in the nomenclature). The isotherm and streamline maps for the same parameters but for $\kappa = 0.452$ are shown in Fig. 5. It can be seen that the isotherms and streamlines are symmetric about the vertical center line for pure convection case as well as with the interaction of radiation.

Figs. 4 and 5 show that the strength of the circulation increases with Grashof number and the center of rotation moves further up for both pure convection and for combined transfer modes. An examination of the isotherms reveals that a temperature inversion exists in part of the region between the two boundary layers with the fluid near the cold outer surface being warmer than that closer to the hot inner surface. The fluid at the lower portion of the annulus is practically stagnant. At $Gr = 10^9$, the recirculation regions lie closer to the upper part of the outer boundary. The flow in the circular annulus is found to be always bicellular for the parametric range considered.

While comparing the pure convection and combined transport cases, it can be noticed that the isotherms in the solid are less dense for pure convection case as compared to those with radiation. This can be traced to the homogenization of the temperature in the fluid due to the effect of radiation. Less refraction is observed in the isotherms at the solid–fluid interface for the combined transfer cases at all Grashof numbers.

The variations in the isotherm and streamline patterns with Grashof number in the fluid region are found to be similar for other thermal conductivity ratios. At lower thermal conductivity ratio, the isotherms in the solid become denser compared to those in the fluid region at higher Grashof numbers. However, at higher thermal conductivity ratio, temperature homogenization occurs even at lower Grashof numbers. For all values Gr, a refraction is observed in the isotherms at the solid–fluid interface which is in accordance with the heat flux continuity condition.

4.2. Variation of vertical velocity profiles along the horizontal mid-plane

Fig. 6a and b shows the vertical velocity profiles at mid-height (i.e., the variation of v_θ^* at $\theta = 0$ with respect to r^*) for $\lambda_s^* = 10$, $\kappa = 0.226$ for $Gr = 10^8$ and $Gr = 10^9$, respectively, for $\epsilon = 0.4$ and $\epsilon = 0.0$ (pure convection). It can be observed that radiation not only reduces the peak velocities but also modifies the velocity profile in the core of the annulus. This can be traced to the fact that, compared to pure natural convection case, the radiation reduces

Table 2
Comparison of the steady-state results obtained using three algorithms in the horizontal annulus for $Gr = 10^8$ and $\lambda_s^* = 10$ and 50.

λ_s^*	κ	Algorithm	$T^*_{\text{pnc,max}}$	$T^*_{\text{pnc,av,ib}}$	$Nu_{\text{pnc,av,ib}}$	$Nu_{\text{pnc,av,ob}}$
10	0.226	P	0.00936	0.00802	14.06	3.24
		A	0.00933	0.00799	14.11	3.19
		D	0.00934	0.00800	14.08	3.21
10	0.452	P	0.02337	0.0180	12.53	5.81
		A	0.02321	0.0178	12.61	5.52
		D	0.02331	0.0179	12.56	5.66
50	0.226	P	0.00840	0.00812	13.89	3.19
		A	0.00831	0.00804	13.88	3.16
		D	0.00839	0.00811	13.89	3.18
50	0.452	P	0.0196	0.0184	12.25	5.66
		A	0.0195	0.0183	12.30	5.47
		D	0.0195	0.0183	12.27	5.58

P, Perić et al. [20]; A, Armfield [21]; D, Date [22,23].

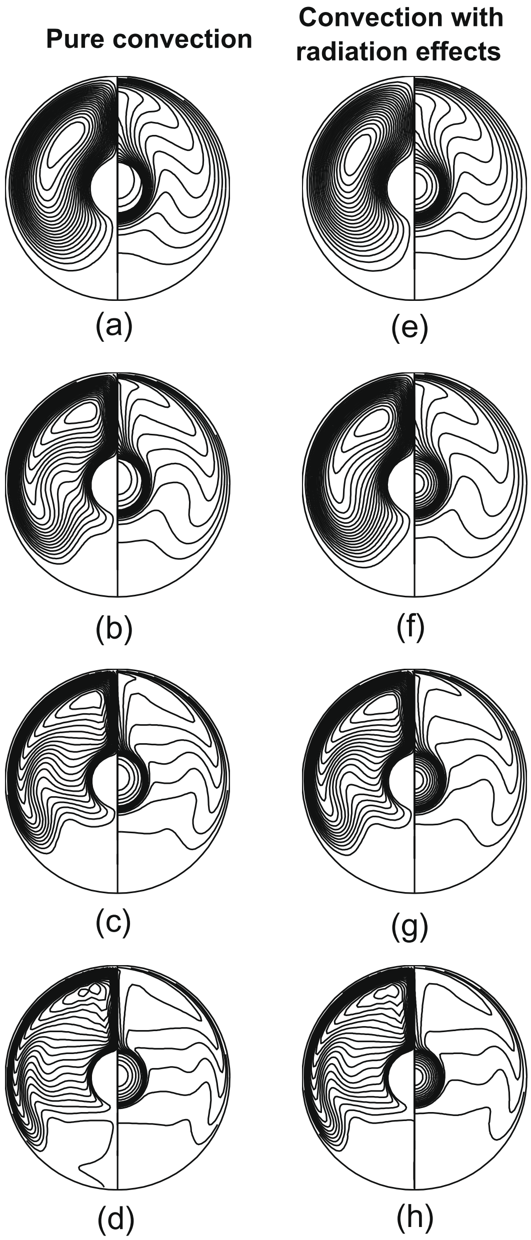

Fig. 4. Isotherm (right half) and streamline (left half) maps for $\lambda_s^* = 10,\ \kappa = 0.226$ and Gr values 10^7 (a and e), 10^8 (b and f), 10^9 (c and g) and 10^{10} (d and h) for pure convection (a–d) and convection with radiation effects (e–h).

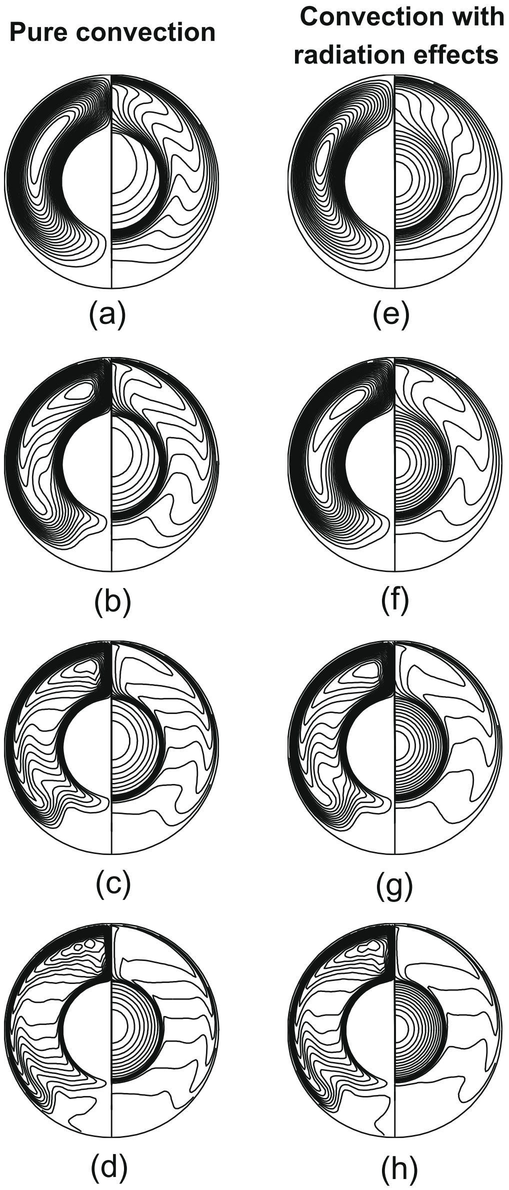

Fig. 5. Isotherm (right half) and streamline (left half) maps for $\lambda_s^* = 10,\ \kappa = 0.452$ and Gr values 10^7 (a and e), 10^8 (b and f), 10^9 (c and g) and 10^{10} (d and h) for pure convection (a–d) and convection with radiation effects (e–h).

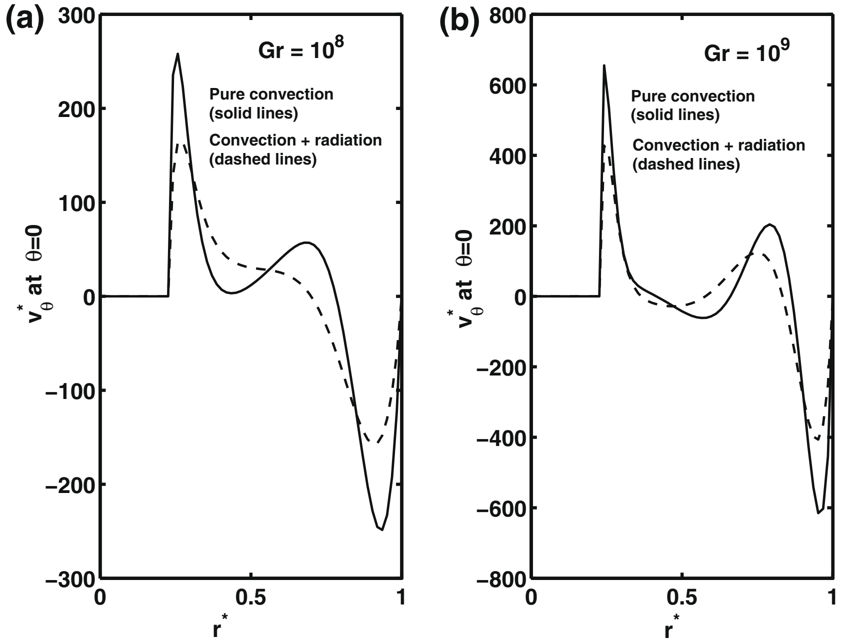

Fig. 6. Vertical velocity profiles at mid-height for $\lambda_s^* = 10,\ \kappa = 0.226,\ \epsilon = 0.4$ and $\epsilon = 0.0$ for (a) $Gr = 10^8$ and (b) $Gr = 10^9$.

the temperatures while also tending to even out the temperature distribution in the fluid.

4.3. Variation of average Nusselt number with Grashof number

The convective Nusselt number ($Nu_{\mathrm{c,av,ib}}$), radiative Nusselt number ($Nu_{\mathrm{r,av,ib}}$) and maximum dimensionless temperature (T^*_{max}) obtained with the interaction of radiation with surface emissivities of the inner and outer boundaries taken as $\epsilon = 0.6$ are compared with the pure natural convective values ($Nu_{\mathrm{pnc,av,ib}}$ and $T^*_{\mathrm{pnc,max}}$) for Gr ranging from 10^7 to 10^{10}, $\kappa = 0.226$ and 0.452 and λ_s^* of 5 and 10 in Tables 3 and 4. It is noticed that the maximum temperatures attained are lower for cases with the radiation effects than for pure convection cases because of the increased radiative Nusselt numbers due to radiation. Also, the average convective Nusselt numbers on the inner boundary reduces compared to the pure natural convection case, when radiation effects are considered. This phenomenon is referred to as the convective drop (for instance, Balaji and Venkateshan [10]). This can be seen clearly in Fig. 7, which shows the variation of the average Nusselt numbers on the inner boundary for pure convection case ($Nu_{\mathrm{pnc,av,ib}}$) and for convection with the radiation effects ($Nu_{\mathrm{c,av,ib}}$) for $\kappa = 0.226$ and 0.452 and $\lambda_s^* = 10$. Fig. 7 shows that surface radiation leads to a drop in the convective component by 9–15% as compared to the pure convection ($\epsilon = 0.0$) case. This is due to the fact that radiation equilibrates the temperature in the fluid region. Since the convective Nusselt number drops, the rest of the contribution to the total Nusselt number comes from surface radiation. It is found that radiative Nusselt numbers are about 60–70% of the total Nusselt numbers. As expected, $Nu_{\mathrm{c,av,ib}}$ for $\kappa = 0.226$ is found to be higher as compared to $\kappa = 0.452$ due to less space available for the convective movement. It is also observed that $Nu_{\mathrm{c,av,ib}}$ does not vary much with λ_s^* beyond 10.

Table 3
Comparison of the convective and radiative Nusselt numbers in the horizontal annulus for $\epsilon = 0.6,\ \lambda_s^* = 5$ and 10.

λ_s^*	κ	Gr	$T^*_{\mathrm{pnc,max}}$	$Nu_{\mathrm{pnc,av,ib}}$	T^*_{max}	$Nu_{\mathrm{c,av,ib}}$	$Nu_{\mathrm{r,av,ib}}$	Nu_{t}
5	0.226	10^7	0.0150	9.18	0.0107	8.28	12.12	20.4
		10^8	0.0106	14.17	0.00769	12.66	28.39	41.05
		10^9	0.0076	22.14	0.00625	18.24	32.09	50.33
		10^{10}	0.0061	31.66	0.00542	28.58	34.42	63.0
5	0.452	10^7	0.0392	7.93	0.0195	5.67	18.54	24.21
		10^8	0.0282	12.66	0.0217	11.14	28.51	39.65
		10^9	0.0214	20.27	0.0125	16.58	31.31	47.89
		10^{10}	0.0177	30.22	0.0096	26.32	33.44	59.76
10	0.226	10^7	0.0138	9.10	0.0070	7.55	12.13	19.68
		10^8	0.0093	14.06	0.0041	10.93	28.35	39.58
		10^9	0.0064	22.02	0.0035	18.03	32.00	50.47
		10^{10}	0.0048	31.58	0.0031	28.16	34.32	62.48
10	0.452	10^7	0.0345	7.82	0.0144	5.64	18.55	24.19
		10^8	0.0233	12.53	0.0111	9.26	28.49	37.75
		10^9	0.0164	20.11	0.0099	15.96	30.44	46.4
		10^{10}	0.0126	30.11	0.0088	26.21	33.44	59.65

Table 4
Comparison of the dimensional temperatures for $\kappa = 0.452$, $\lambda_s^* = 5$ from ϵ = 0.0–0.8 for $T_{\text{ref}} = 300\,K$.

ϵ	Gr	$\dot{Q}_v$ (W m^{-3})	ΔT (°C)	$T^*_{\max}$	$T_{\max}$ (°C)
0.0	10^9	719.0	1069.1	0.0214	67.33
	5×10^9	3595.0	5220.3	0.0194	156.85
	10^{10}	7190	10691.0	0.0177	251.58
0.4	10^9	719.0	1069.1	0.0147	50.73
	5×10^9	3595.0	5345.3	0.0123	100.94
	10^{10}	7190	10691.0	0.0114	157.41
0.6	10^9	719.0	1069.1	0.0125	48.27
	5×10^9	3595.0	5345.3	0.0104	90.81
	10^{10}	7190	10691.0	0.0096	138.74
0.8	10^9	719.0	1069.1	0.0108	43.98
	5×10^9	3595.0	5345.3	0.0091	83.42
	10^{10}	7190	10691.0	0.0084	124.85

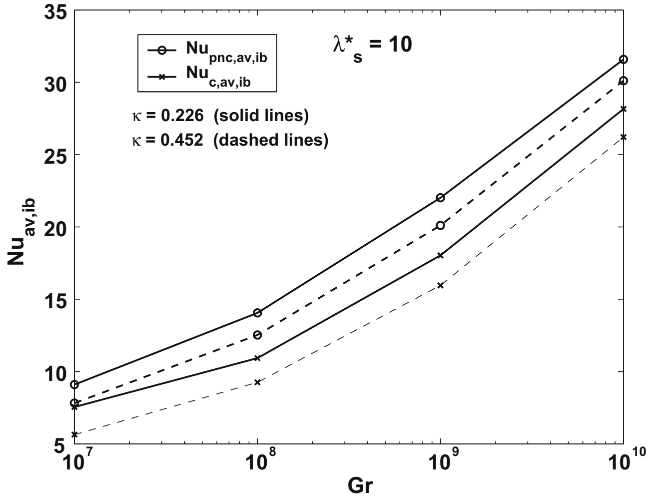

Fig. 7. Variation of the average Nusselt numbers with Grashof number for pure convection ($\epsilon = 0.0$) and convection with radiation effect ($\epsilon = 0.6$) for $\lambda_s^* = 10$ and for $\kappa = 0.226$ and 0.452.

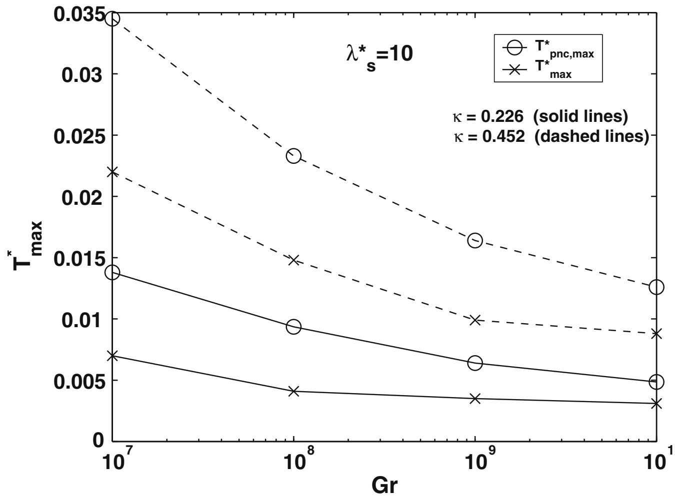

Fig. 8. Variation of the dimensionless maximum temperature with Grashof number for pure convection ($\epsilon = 0.0$) and convection with radiation effect ($\epsilon = 0.6$) for $\lambda_s^* = 10$ and $\kappa = 0.226$.

4.4. Variation of dimensionless maximum temperature with Grashof number

Fig. 8 shows the variation of dimensionless maximum temperature in the solid in case of pure convection ($\epsilon = 0.0$) and with the radiation effects ($\epsilon = 0.6$), for $\kappa = 0.226$ and 0.452 for $\lambda_s^* = 10$. It can be observed that $T^*_{\text{pnc,max}}$ values are higher than those of $T^*_{\max}$, which take into account the radiation effects. This confirms the fact that increase in the radiation Nusselt numbers lowers the maximum temperatures in the solid. Secondly, since the convection is less at higher radius ratio, $T^*_{\max}$ is higher for $\kappa = 0.452$ compared to the case of $\kappa = 0.226$.

4.5. Effect of the surface emissivity

To study the effect of the emissivity of the surfaces on the heat transfer characteristics, results are computed for four emissivities between 0.2 and 0.8, for $\lambda_s^* = 10$ and $\kappa = 0.226$. Fig. 9 shows the variation of the average convection Nusselt numbers on the inner boundary with Grashof number for $\epsilon = 0.0$ (pure convection case) to $\epsilon = 0.8$. It can be clearly seen that the convective drop increases

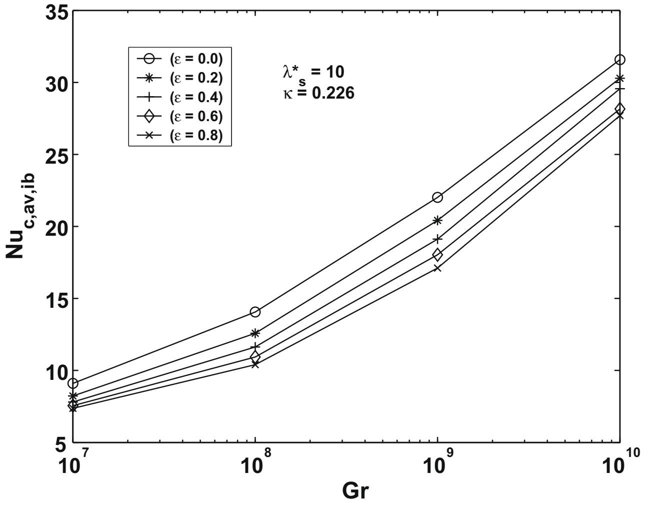

Fig. 9. Variation of the average convection Nusselt numbers with Grashof number for ϵ = 0.2–0.8 for $\lambda_s^* = 10$ and $\kappa = 0.226$.

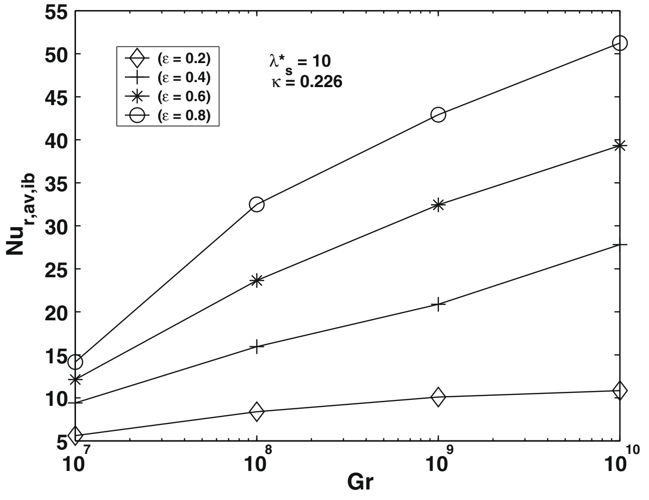

Fig. 10. Variation of the average radiation Nusselt numbers with Grashof number for ϵ = 0.2–0.8 for $\lambda_s^* = 10$ and $\kappa = 0.226$.

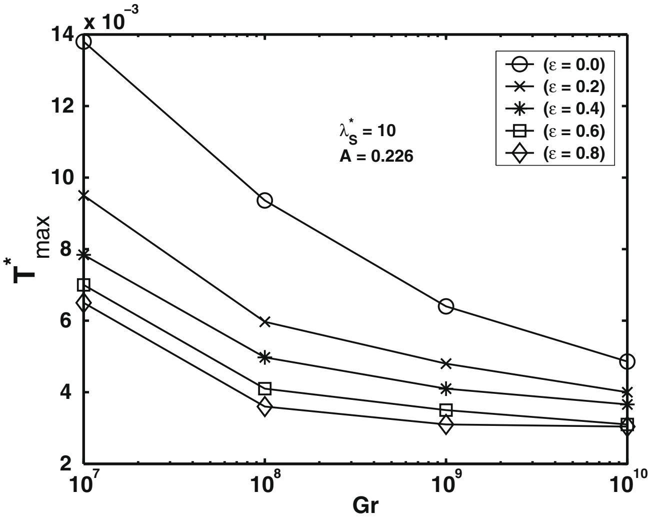

Fig. 11. Variation of the dimensionless maximum temperature with Grashof number for ϵ = 0.0–0.8 for $\lambda_s^* = 10$ and $\kappa = 0.226$.

with the emissivity of the surfaces. Fig. 10 shows the variation of the average radiation Nusselt number on the inner boundary with Grashof number for $\epsilon = 0.2,\ 0.4,\ 0.6$ and 0.8. It is observed that the radiation Nusselt number increases with the emissivity as expected. Fig. 11 shows the variation of the dimensionless maximum temperatures with *Gr* for $\epsilon = 0.0$ (pure convection case) to $\epsilon = 0.8$. It is evident from the figure that the dimensionless maximum temperatures are significantly high for the pure convection case compared to the combined transfer case, since the increased radiation Nusselt numbers reduces the temperatures in the solid cylinder.

5. Correlations for the combined heat transfer case

The correlations for the dimensionless maximum temperature ($T_{\max}^*$), average solid cylinder temperature ($T_{\mathrm{av,s}}^*$), average convective Nusselt number on the inner boundary ($Nu_{\mathrm{c,av,ib}}$) and the average radiative Nusselt number on the inner boundary ($Nu_{\mathrm{r,av,ib}}$) from the computed data are given in Table 5 for radius ratios of $\kappa = 0.226$ and 0.452. In correlating the effect of emissivity, the functional form $(1+\epsilon)$ or $(1+\epsilon^a)$ (where a is a suitable exponent) is used to obtain the best possible correlation. It may be noted that this quantity becomes unity as ϵ tends to unity (pure natural convection). The table gives information about the radius ratio (κ), the functional form, mean square error (e_{ms}) and the correlation coefficient (C_c) as defined in the nomenclature. Sample parity plots for $T_{\max}^*$ are shown in Figs. 12 and 13 for radius ratios 0.226 and 0.452, respectively.

Table 5
Correlations for $T_{\max}^*$, $T_{\mathrm{av,s}}^*$, $Nu_{\mathrm{c,av,ib}}$ and $Nu_{\mathrm{r,av,ib}}$ for conjugate natural convection with surface radiation ($Pr = 0.7$).

κ	Correlation	e_{ms}	C_c
0.226	$T_{\max}^* = 0.1584Gr^{-0.1291}\lambda_s^{*-0.1689}(1+\epsilon^{0.8277})^{-1.2877}$	0.020	0.9689
	$T_{\mathrm{av,s}}^* = 0.1550Gr^{-0.1424}\lambda_s^{*-0.0968}(1+\epsilon^{0.8448})^{-1.4483}$	0.0165	0.9678
	$Nu_{\mathrm{c,av,ib}} = 0.4093Gr^{0.1916}\lambda_s^{*-0.0047}(1+\epsilon)^{-0.3840}$	0.0012	0.9977
	$Nu_{\mathrm{r,av,ib}} = 1.2\times10^{-4}Gr^{0.1108}\lambda_s^{*-0.0289}(1+\epsilon^{0.15})^{15.488}$	0.0592	0.9982
0.452	$T_{\max}^* = 0.3682Gr^{-0.1089}\lambda_s^{*-0.2709}(1+\epsilon^{0.84})^{-1.3854}$	0.0280	0.9625
	$T_{\mathrm{av,s}}^* = 0.3272Gr^{-0.1244}\lambda_s^{*-0.1746}(1+\epsilon^{0.8783})^{-1.5496}$	0.0216	0.9603
	$Nu_{\mathrm{c,av,ib}} = 0.2378Gr^{0.2154}\lambda_s^{*-0.0098}(1+\epsilon^{0.80})^{-0.4947}$	0.0016	0.9975
	$Nu_{\mathrm{r,av,ib}} = 3.31\times10^{-4}Gr^{0.0586}\lambda_s^{*-0.0004}(1+\epsilon)^{15.9234}$	0.0064	0.9956

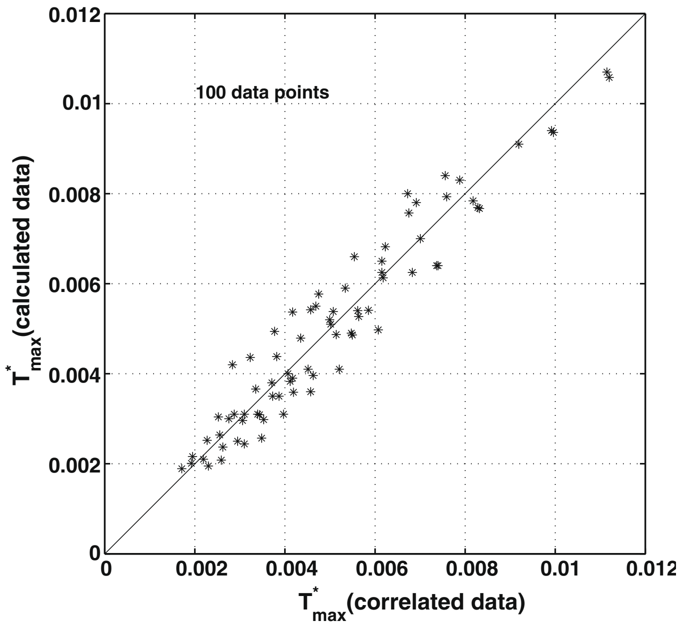

Fig. 12. Parity plot to compare $T_{\max}^*$ (correlated) and $T_{\max}^*$ (calculated) for $\kappa = 0.226$.

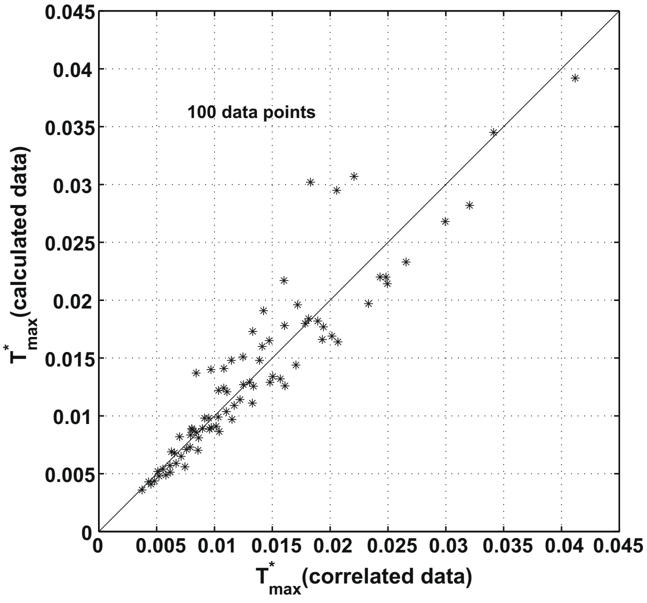

Fig. 13. Parity plot to compare $T_{\max}^*$ (correlated) and $T_{\max}^*$ (calculated) for $\kappa = 0.452$.

6. Conclusions

The following conclusions are reached in the present study.

- In general, the flow and the thermal fields are symmetric about the vertical centerline.
- A refraction of isotherms occurs at the solid–fluid interface and the degree of refraction is found to be higher for higher thermal conductivity ratios.
- The temperature gradients in the solid reduce with an increase in the thermal conductivity ratio, leading to increased homogenization of temperature in the solid.
- The flow in the annulus is always bicellular in the annular space.

- Radiation not only reduces the magnitudes of the vertical velocities but also modifies the velocity profiles in the core of the annulus.
- The stagnant region at the bottom of the annulus is found to increase with Grashof number.
- The degree of refraction of the isotherms at the solid–fluid interface is lower when radiation is considered due to the homogenization of the fluid temperature.
- The dimensionless maximum temperature, obtained by solving the conjugate problem is much lowered with the effect of radiation as compared to the pure convection case, which strengthen the fact that radiation has a significant effect on the solid temperature distribution even at low surface emissivity.
- The surface radiation dampens the convection in the annulus due to the tendency of temperature equilibration in the fluid region. At an emissivity value of 0.6 for instance, the radiative Nusselt numbers are about 50–60% of the total Nusselt numbers depending on the radiative parameters. This factor emphasizes the need for the coupling of radiation and natural convection for the accurate prediction of the flow and heat transfer characteristics.

References

[1] T.H. Kuehn, R.J. Goldstein, An experimental and theoretical study of natural convection in the annulus between horizontal concentric cylinders, J. Fluid Mech. 100 (4) (1976) 695–719.

[2] T.H. Kuehn, R.J. Goldstein, An experimental study of natural convection heat transfer in concentric and eccentric horizontal cylindrical annuli, Trans. ASME J. Heat Transfer 100 (1978) 638–640.

[3] T.H. Kuehn, R.J. Goldstein, A parametric study of Prandtl number and diameter ratio effects on natural convection heat transfer in horizontal cylindrical annuli, Trans. ASME J. Heat Transfer 102 (1980) 768–770.

[4] T.H. Kuehn, R.J. Goldstein, Correlating equations for natural convection heat transfer between horizontal circular cylinders, Int. J. Heat Mass Transfer 19 (1976) 1127–1134.

[5] U. Grigull, W. Hauf, Natural convection in horizontal cylindrical annuli, in: Proceedings of the Third International Heat Transfer Conference, vol. 2, 1966, pp. 154–158.

[6] Z. Rotem, Conjugate free convection from horizontal conducting cylinders, Int. J. Heat Mass Transfer 15 (1972) 1679–1693.

[7] V.I. Bubnovich, P.M. Kolesnikov, Conjugate transient heat transfer in laminar natural convection in a horizontal cylindrical annulus, J. Eng. Phys. 19 (1986) 1175–1181.

[8] P.M. Kolesnikov, V.I. Bubnovich, Non-stationary conjugate free-convective heat transfer in horizontal cylindrical coaxial channels, Int. J. Heat Mass Transfer 31 (6) (1988) 1149–1156.

[9] M. Lacroix, A. Joyeux, Coupling of wall conduction with natural convection from heated cylinders in a rectangular enclosure, Int. Commun. Heat Mass Transfer 23 (1) (1996) 143–151.

[10] C. Balaji, S.P. Venkateshan, Interaction of surface radiation with free convection in a square cavity, Int. J. Heat Fluid Flow 14 (3) (1993) 260–267.

[11] C. Balaji, S.P. Venkateshan, Combined conduction, convection and radiation in a slot, cavity, Int. J. Heat Fluid Flow 14 (1995) 260–267.

[12] N. Ramesh, W. Merzkirch, Combined convection and radiation heat transfer in side-vented open cavities, Int. J. Heat Fluid Flow 22 (2001) 180–187.

[13] S.N. Singh, S.P. Venkateshan, Numerical study of natural convection with surface radiation in side-vented open cavities, Int. J. Therm. Sci. 43 (2004) 865–876.

[14] K.S. Anil, K. Velusamy, C. Balaji, S.P. Venkateshan, Conjugate turbulent natural convection with surface radiation in air filled rectangular enclosures, Int. J. Heat Mass Transfer 50 (2007) 625–639.

[15] M. Perlmutter, J.R. Howell, Radiant transfer through a gray gas between concentric cylinders using Monte Carlo, Trans. ASME J. Heat Transfer 39 (1963) 169–179.

[16] S.O. Onyegegbu, Heat transfer inside a horizontal cylindrical annulus in the presence of thermal radiation and buoyancy, Int. J. Heat Mass Transfer 29 (5) (1986) 659–671.

[17] R.D. Manteufel, N.E. Todreas, Analytic formulae for the effective conductivity of a square or hexagonal array of parallel tubes, Int. J. Heat Mass Transfer 31 (4) (1994) 647–657.

[18] H.C. Hottel, Radiant-heat transmission, in: W.H. McAdams (Ed.), Heat Transmission, third ed., McGraw-Hill, New York, 1954 (Chapter 4).

[19] H.C. Hottel, A.F. Sarofim, Radiative Heat Transfer, McGraw-Hill, New York, 1967.

[20] M. Perić, R. Kessler, G. Scheuerer, Comparison of finite-volume numerical methods with staggered and collocated Grids, Comput. Fluids 16 (4) (1988) 389–403.

[21] S.W. Armfield, Finite difference solutions of the Navier–Stokes equations on staggered and non-staggered grids, Comput. Fluids 20 (1) (1991) 1–17.

[22] A.W. Date, Fluid dynamical view of pressure checkerboarding problem and smoothing pressure correction on meshes with colocated variables, Int. J. Heat Mass Transfer 46 (2003) 4885–4898.

[23] A.W. Date, Introduction to Computational Fluid Dynamics, Cambridge University Press, New York, 2005.

[24] K.E. Torrance, J.A. Rockett, Numerical study of natural convection in an enclosure with localized heating from below creeping flow to the onset of laminar instability, J. Fluid Mech. 36 (1969) 33–54.

[25] K. Vafai, J. Ettefagh, Thermal and fluid flow instabilities in buoyancy-driven flows in open-ended cavities, Int. J. Heat Mass Transfer 33 (10) (1990) 2329–2344.

[26] P.J. Roache, Fundamentals of Computational Fluid Dynamics, Hermosa Publishers, Albuquerque, New Mexico, 1998.

[27] P.E. Gill, G.F. Miller, An algorithm for the integration of the unequally spaced points, Comput. J. 15 (1972) 80–83.

[28] G. de Vahl Davis, Natural convection of air in a square cavity: a bench mark numerical solution, Int. J. Numer. Meth. Fluids 3 (1983) 249–264.

[29] M. Hortmann, M. Peric, G. Scheuerer, Finite volume multigrid prediction of laminar natural convection: bench-mark solutions, Int. J. Numer. Meth. Fluids 11 (1990) 189–207.